Design and Validation of a CT- and MRI-Guided Robot for Percutaneous Needle Procedures

Nikolai Hungr, Ivan Bricault, Philippe Cinquin, and Céline Fouard

***Abstract*—This paper describes the design and evaluation of the second generation of a robotic system called the light puncture robot for thoracic and abdominopelvic interventional radiology procedures under CT and MRI guidance. It is mounted on the patient's body and positions and inserts the needle according to the trajectory and target chosen by the radiologist in the image. The mechanical design is described in detail along with its forward and inverse kinematics. The robot can be segmented and registered fully automatically in both imaging modalities. Phantom experiments in the CT scanner and preliminary feasibility experiments in the MRI are described, showing a targeting accuracy of 3.3 ± 1.7 mm in gelatin for depths ranging from 30 to 90 mm and needle orientations of –13° to +15° about normal from the patient's skin. A detailed error analysis is discussed along with potential improvements in the system. The potential clinical advantages of the system include higher targeting accuracy for complex dual obliquity trajectories, the need for fewer images, and improved accessibility to MRI-guided interventions.**

***Index Terms*—Biopsy, CT, interventional radiology (IR), medical robotics, MRI, parallel robots, robot kinematics.**

I. Introduction

ROBOTICS in the field of interventional radiology (IR), and, in particular, in the context of CT- and MRI-guided percutaneous needle procedures is a well-established field of research with numerous systems published in the literature worldwide since the beginning of the century. Percutaneous interventions are minimally invasive clinical procedures that involve the insertion of needles through a patient's skin for diagnostic or therapeutic purposes. Specific examples of such procedures are biopsies, tumor ablations, abscess drainages, and drug administration. Compared with surgical interventions, their particularity is that they rely on medical imaging for the planning and execution of the needle trajectory.

Because of the lack of direct visibility of the clinical target, which tends to be relatively small, clinicians are faced with a number of difficulties that make the procedure particularly adapted to robotics. The challenge generally lies in the need to mentally reproduce the needle trajectory that was planned in the control room on the patient's body in the imaging room. Numerous control images are typically required to ensure that the needle is in line, in particular for complex trajectories involving dual obliquities and nearby vital structures such as blood vessels, nerves, and bones. In order to simplify the task, radiologists generally tend to keep the needle trajectories in the transverse imaging plane and close to vertical. The high accuracy and stability that can be attributed to robots, coupled to image analysis techniques, could provide clinicians with the ability to reach clinical targets through a greater variety of trajectory corridors, with the need for fewer control images. In this paper, we describe a CT- and MRI-guided needle puncture robot for abdominal and thoracic procedures that we have named the Light Puncture Robot (LPR).

A. Existing Needle Insertion Robots

Table I shows a summary of all the CT- and MRI-guided thoracic and abdominal IR robots that we were able to compile from the recent scientific literature. These robots are all typically designed to insert a needle through the patient's skin anywhere in the upper body without necessarily being constrained to a certain organ.

In Table I, we can see that existing systems vary significantly in their robotic architectures, degrees of freedom (DOF), actuation types, and levels of automation. They are, however, all dictated by the same set of general constraints. One of the main constraints is their necessary reliance on medical imaging for guidance. CT- and MRI-guided robots are particularly constrained in their design due to the size constraints of the standard 60 or 70 cm scanner bore diameter as well as material compatibility constraints, with high density, ferromagnetic and conductive materials typically being incompatible. Material compatibility is especially challenging in the MRI, as ferromagnetic materials must not only be present in the field of view of the image, but as well as in the surrounding proximity of the imager.

The use of medical imaging for guidance means that the robots must be registered to the image space in order to be able to send appropriate displacement commands. In MRI and CT scanners, this is most often done using fiducials or known shapes that are visible in the image. For example, in the MRI, hollow shapes filled with the gadolinium contrast agent can be used [1]–[3].

Other constraints are derived from the percutaneous nature of the procedures. Accuracies must be high because the targets tend to be millimetric for insertion depths of up to 15 to 20 cm.

Manuscript received July 21, 2015; revised December 18, 2015; accepted April 13, 2016. Date of publication August 02, 2016; date of current version August 18, 2016. This paper was recommended for publication by Associate Editor C. Secchi and Editor B. J. Nelson upon evaluation of the reviewers' comments. This work was supported in part by the French Agence Nationale de la Recherche.

N. Hungr and C. Fouard are with the Laboratoire TIMC-IMAG, Equipe GMCAO, La Tronche 38706, France (e-mail: Nikolai.Hungr@imag.fr; Celine.Fouard@imag.fr).

I. Bricault is with the CHU de Grenoble, La Tronche 38700, France (e-mail: IBricault@chu-grenoble.fr).

P. Cinquin is with the Laboratoire TIMC-IMAG, Equipe GMCAO, La Tronche 38706, France, and also with the CHU de Grenoble, La Tronche 38700, France (e-mail: Philippe.Cinquin@imag.fr).

Color versions of one or more of the figures in this paper are available online at http://ieeexplore.ieee.org.

Digital Object Identifier 10.1109/TRO.2016.2588884

TABLE I
EXISTING ROBOTS FOR PERCUTANEOUS THORACIC AND ABDOMINAL INTERVENTIONS

Institution	Project Name	Status	Imaging Modality	Actuation Technology	Robot Position	DOF	Needle Insertion	Reported Accuracy			References
								Accuracy (mm)	Needle Depth (mm)	Test Medium	
Johns Hopkins University	B-ROB / iSYS	C	US / CT	Motor	Table-mounted	4	Manual	1.1	85	Foam phantom	[6], [15]–[19]
Johns Hopkins University	PAKY / RCM / AcuBot	C	CT / US / Fluor.	Motor	Table-mounted	6	Robotic	1.2	–	Agar phantom	[20]–[28]
University of Freiburg	–	P	CT	Motor	Table-mounted	2	Manual	1.6	75	In vitro pig organs	[29]
Innomedic	Innomotion	C	MRI / CT	Pneumatic	Table-mounted	5	Manual	1	(40–70)	In vivo pig	[2], [30]–[33]
KIOS Research Center	–	P	MRI	Manual	Table-mounted	6	Manual	<5	-40	Butter phantom	[3]
Washington University	-	P	MRI	Piezo motor	Table-mounted	7	Manual	–	–	–	[34]–[37]
Worcester Polytechnic Institute	-	P	MRI	Piezo motor	Table-mounted	6	Manual	–	–	–	[38]–[40]
LSIIT (ICUBE)	CT-Bot	A	CT	Piezo motor	Patient-mounted	5	Manual	<5	65	Artificial phantom	[41]–[45]
MIT	Robopsy	A	CT / MRI	Motor / Piezo Motor	Patient-mounted	3	Robotic	(<20)	-80	In vivo pig	[5], [46], [47]
TIMC Laboratory	LPR	A	CT / MRI	Pneumatic	Patient-mounted	5	Robotic	<2 mm	100	Foam phantom	[7]–[9]

The project status is either clinical patient tests (C), live animal tests (A) or phantom tests (P). The precision and needle depth values in parentheses are values that are not specifically stated in the publications but are rather estimates taken from images or textual hints. US motor stands for ultrasonic motor.

Although needle insertion forces are relatively low, typically remaining below 20 N [4], when combined with the size and material constraints imposed by the medical environment, appropriate robot architecture design becomes challenging to ensure sufficient structural rigidity, and consequently, provide the high accuracies required at the needle tip.

Needle insertion robots are all composed of at least two modules: a needle positioning module and an insertion module. The positioning module necessarily requires four to five DOFs to be able to position the needle tip at the skin entry point and orient the needle shaft along the planned insertion direction. Once the needle is in position, the insertion module needs at least one DOF to push the needle toward the internal target.

The robots in Table I use varying degrees of actuation for these DOFs with consequential benefits and limitations. The robot described in [5], for example, only actuates the two orientation DOFs of the positioning module, meaning that the needle tip must be placed at the skin entry point manually. This allows the architecture to be significantly lightened but requires careful planning to ensure correct initial alignment. Other robots, such as [6] and [2], do not actuate the insertion module, allowing the surgeon to insert the needle manually. This simplifies the risk analysis for use on humans but does not allow in-bore insertions or controlled insertion schemes, for example.

Another important design aspect is robot fixation. Robots can be fixed either to the scanner bed, as in the majority of the existing designs, or they can also be fixed to the patient. Table-fixation provides a rigid platform that is less likely to move between image sequences. It also allows the robot to be registered directly to the scanner's workspace. Patient fixation is typically more complex, as it requires a careful balance between rigidity and patient comfort. But this method tends to be less space consuming and allows the patient to move between image sequences, an important consideration for procedures that can take up to several hours.

B. Context and Clinical Goals

The LPR robot that we describe in this paper is a second prototype in a project that has been ongoing since 2004. The previous prototype, as described in a number of prior articles [7]–[9], consisted of a three-DOF needle insertion module (two orientations + one insertion) placed directly in contact with the patient's body and strapped to the four corners of a surrounding bed-mounted frame. Novel pneumatic motors were used to shorten and lengthen the respective straps in order to provide two additional DOFs to position the needle above the chosen skin entry point.

The first prototype design was successfully used on phantom and live pig trials with a targeting accuracy of less than 2 mm. However, it had a number of limitations that made it impractical for clinical use. The bed-mounted frame was found to significantly limit the size of the patient on which the system could be used. The pneumatic motors, although accurate and completely MRI-compatible, were slow and moved in incremental amounts, limiting the robot's resolution. Ultimately, however, the most important limitation was that it was impractical to sterilize.

For this reason, the second prototype, first presented in [10] and [11] and described in detail here, was a significant change to the original design. The primary advantages of the first prototype were maintained, in particular the body-mounted

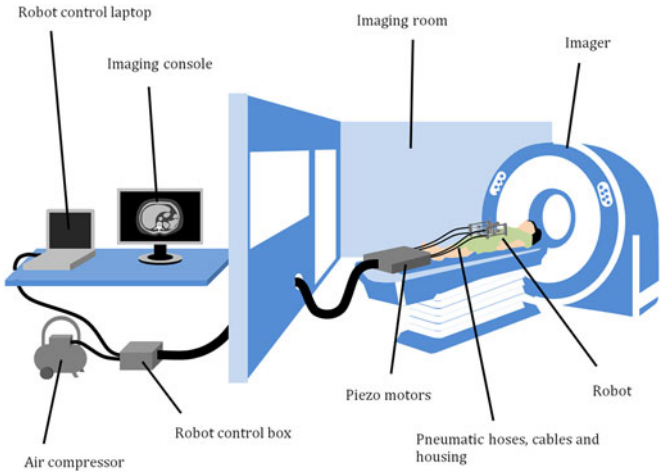

Fig. 1. General layout of the various components of the LPR system within the imaging room.

configuration, pneumatic grip-based needle insertion, fiducial-based registration, and multimodal CT and MRI compatibility.

The clinical goal of the LPR robot is to provide increased needle targeting accuracy with greater ease and fewer image acquisitions, in particular for difficult, dual-obliquity, and anatomically constrained insertions (such as between the ribs). The originality of the project, with respect to other robotic systems, is its multimodality and its generic design, adapted to a large spectrum of needle-based IR procedures. This improves its potential clinical value for patients by offering a greater number of possible interventions; for radiologists by allowing them to take advantage of the complementary information provided by CT and MRI scanners; and for hospitals by offering a more generic tool usable in a greater number of situations.

In the following sections, we will describe the LPR v2 in detail, including the kinematics, actuation details, and fiducial segmentation–registration techniques, followed by a preclinical phantom feasibility evaluation in both CT and MRI scanners.

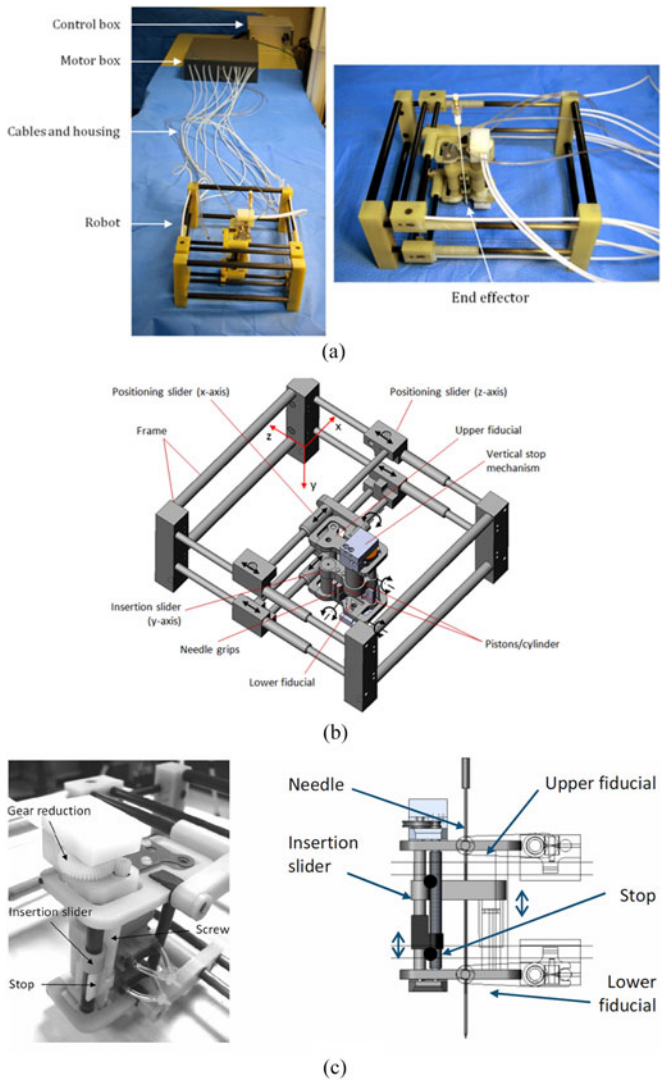

Fig. 2. LPR v2 robot architecture. (a) Photograph of the prototype LPR system (left) and close-up of the robot (right), showing the end effector location at the needle's tip. (b) CAD drawing showing the various components and DOF of the robot. (c) Detailed view of the insertion module, showing the various components that allow the needle to be inserted to a step depth defined by vertically adjustable stop.

II. Materials

A. Robot Description

The LPR v2 robot consists of a number of components, some of which are located inside the imaging room and others in the control room, as shown in Fig. 1. The robot itself holds the needle and is mounted onto a radiology vacuum cushion fixed to the patient's body using flexible straps. The robot is actuated by MRI-compatible ultrasonic motors mounted in a motor box at the patient's feet. The rotational motors pull pairs of Bowden cables that are connected to the various robot joints. This configuration allows the motors to stay outside of the imaging bore, hence, keeping them from affecting the image quality and significantly reducing the weight of the robot on the patient's body. The effect of the proximity of the motor box to the CT and MRI scanner bores on image quality was tested and described in [10]. It was found that the motors do not affect image quality except for a minor reduction in signal-to-noise ratio in the MRI when the motors are in motion. Although this effect was insignificant, it is of no effect to the protocol that will be described below, as the motors are never actuated during image acquisition. The electronics for controlling the motors are susceptible to being affected by and of affecting the MRI and CT machines because of electromagnetic emissions and the presence of ferromagnetic parts. They are, therefore, mounted in a control box that is placed outside of the imaging room. The robot control PC is placed next to the imaging console, allowing rapid transfer of images using a DICOM server. This configuration allows the radiologist to remain in front of the images instead of having to go back and forth between the patient and the control room throughout the procedure.

The five DOF robot architecture, shown in Fig. 2, has the characteristics described in Table II. It is based on two pairs of parallel x and z sliders and an insertion module. The positioning module allows the needle to be translated within a planar x-z

TABLE II
CHARACTERISTICS OF THE LPR V2 PROTOTYPE

WORKSPACE:	
DOF	5
Needle tip workspace above skin (x-z plane)	135 mm × 120 mm
Needle orientation about x-axis	10° to –20°
Needle orientation about z-axis	24° to –32°
Insertion stroke	0 to 35 mm
ACTUATION:	
Positioning module actuation	Four ultrasonic motors + Bowden cables pairs
Insertion depth adjustment	One ultrasonic motor + Bowden cable pair
Insertion actuation	Two pneumatic pistons + Two pneumatic grips
SIZE & WEIGHT:	
Needle diameters	22 G to 15 G (0.7 to 1.8 mm)
Robot weight	1.0 kg
Robot size (L × W × H)	285 mm × 250 mm × 140 mm
MATERIALS:	
Structure	Epoxy resin
Sliders	Carbon fiber
Fiducials	Soft PVC (MRI) + air (CT)
Cables	Kevlar–Dyneema
Cable housing	Teflon
Others	Nylon

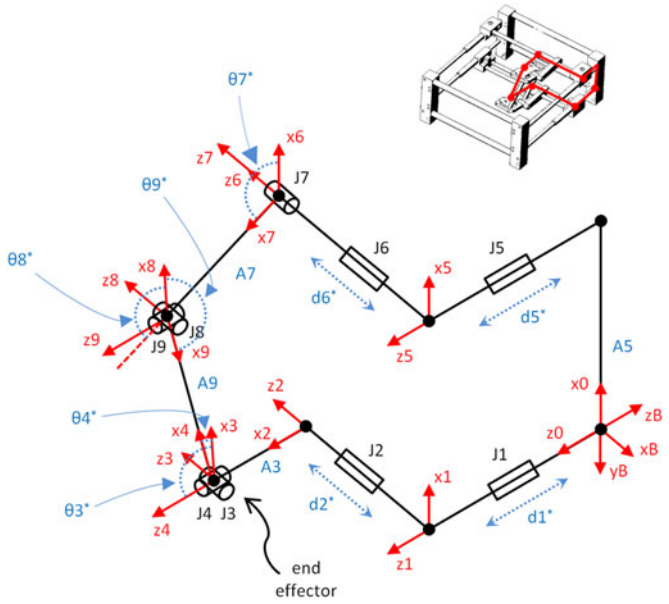

Fig. 3. LPR manipulator kinematic diagram. The letter J represents the robot's various joints. The thetas represent the variable angular positions of the revolute joints. Lowercase d's represent the variable distances attributed to the robot's actuated prismatic joints. Upper case A's represent fixed link lengths. The reference frames attached to each of the manipulator's links are shown in red, with only the x- and z-axes shown. The robot's end effector is located at reference frame 4 but with a –90° rotation about the z-axis such that the y-axis points towards J9. The end effector location can be seen in Fig. 2. Before insertion, the needle tip is located at the end effector.

workspace and oriented about the robot's end effector (located at the needle's tip in the initial home position). The Bowden cables allow the robot to be placed freely anywhere on the patient's abdomen or thorax. The four Shinsei USR60-E3N piezo motors allow fast, smooth, and accurate actuation compared with the first LPR prototype.

The insertion module shown in Fig. 2(c) consists of insertion and withdrawal pistons and two needle grips, all actuated by pneumatic solenoid valves. The mobile upper grip is mounted to the insertion piston and is used to push the needle during insertion. The lower grip is used to hold the needle in place between insertion strokes. Pneumatics was chosen in order to provide enough force for the needle insertion. A fifth ultrasonic motor is used to control a depth stop mounted to a vertical screw and a gear reduction pair, which allows the insertion stroke distance to be adjusted between 0 and 35 mm (measured from the initial prestroke position of the needle tip). A sequence of strokes can thus be done to reach any depth required.

The positioning and insertion modules mounted on the patient's body are both sterilized using a low-temperature hydrogen peroxide plasma technique called STERRAD. This ensures that all the components within reach of the radiologist and needles are sterilized, reducing the risk of accidental contamination. Tests showing the compatibility of the robot with the STERRAD sterilization technique have been described in [10], the conclusion being that all materials are compatible with the sterilizing agent and the robot is small enough to fit into the chamber.

B. Robot Control System

The electronics used to control the robot are contained in a single control box. The main component groups include a digital input/output board for receiving the PC's commands and distributing them to the various components, the Shinsei motor drivers that convert the desired motor speed and direction signals into motor signals, a digital-to-analog converter board to convert the digital control signals to analog voltage required by the Shinsei motor drivers and the pneumatic solenoid valves that control the needle grips and insertion slider. Electrical relays are used to control whether the pneumatic solenoid valves are ON or OFF. The PC communicates with the control box through a single USB cable and the motor connector and pneumatic hose connectors all fit through the 5-cm-diameter control hatches found in the imaging rooms. Since motor speeds are low (<20 r/min) and no force feedback is necessary in this version, simple closed-loop control was used based on the position feedback of the 500-count encoder included with the Shinsei motors.

C. Robot Forward Kinematics

The LPR manipulator's kinematic diagram is shown in Fig. 3. It is based on a parallelogram-type manipulator with two kinematic chains that split at the robot's base and reunite at the robot's end effector.

To determine the forward kinematics, the modified Denavit–Hartenberg (DH) convention, as presented by [12], was used. The DH link parameters are listed in Table III and the transformation between each set of linked reference frames is defined

TABLE III
LPR ROBOT'S DH PARAMETERS

Link(i-1→i)	d_i ($x_{i-1}\rightarrow x_i$ along z_i)	θ_i ($x_{i-1}\rightarrow x_i$ about z_i)	a_{i-1} ($z_{i-1}\rightarrow z_i$ along x_{i-1})	α_{i-1} ($z_{i-1}\rightarrow z_i$ about x_{i-1})
		Chain 1		
B→0	0	90	0	180
0→1	d1*	0	0	0
1→2	d2*	−90	0	-90
2→3	0	θ3*	A3	0
3→4	0	θ4*	0	90
4→ee	0	−90	0	0
		Chain 2		
0→5	d5*	0	A5	0
5→6	d6*	0	0	−90
6→7	0	−θ7*	0	0
7→8	0	θ8*	A7	0
8→9	0	−θ9*	0	90
9→4	0	180	A9	0

Angles θ and α are written in degrees. Asterisks denote the mobile joint variables. All other values are constant regardless of the robot's pose. ee stands for end effector.

by the equation

$$T_{i-1,i} = \begin{bmatrix} \cos\theta_i & -\sin\theta_i & 0 & a_{i-1} \\ \sin\theta_i \cos\alpha_{i-1} & \cos\theta_i \cos\alpha_{i-1} & -\sin\alpha_{i-1} & -\sin\alpha_{i-1} d_i \\ \sin\theta_i \sin\alpha_{i-1} & \cos\theta_i \sin\alpha_{i-1} & \cos\alpha_{i-1} & \cos\alpha_{i-1} d_i \\ 0 & 0 & 0 & 1 \end{bmatrix} \quad (1)$$

where *i* is the current frame and *i*–1 is the previous frame in the kinematic chain. The equations for the robot's two kinematic chains are given below:

Chain 1:

$$T^1_{\mathrm{Bee}}(d_1^*, d_2^*, \theta_3^*, \theta_4^*) = \mathrm{T_{B0}} \cdot \mathrm{T_{01}} \cdot \mathrm{T_{12}} \cdot \mathrm{T_{23}} \cdot \mathrm{T_{34}} \cdot \mathrm{T_{4ee}}. \quad (2)$$

Chain 2:

$$T^2_{\mathrm{Bee}}(d_5^*, d_6^*, \theta_7^*, \theta_8^*, \theta_9^*) = T_{B0} \cdot T_{05} \cdot T_{56} \cdot T_{67} \cdot T_{78} \cdot T_{89} \cdot T_{94} \cdot T_{4ee}. \quad (3)$$

The robot has four actuated prismatic joints (d^*) and five passive revolute joints (θ^*). Instead of solving the complex system of nonlinear equations that result from equating the two kinematic chains, the five unknown revolute joints can be determined by using inspection of the manipulator's geometry. The approach, illustrated in Fig. 4, involves first calculating the location of frames 3 and 7 from the DH link transformations of each respective kinematic chain and then locating frame 9 by finding the intersection between the circle of constant radius A7 and the sphere of constant radius A9.

To find the unknown joint angles $\theta 3$ and $\theta 4$, we first find the positions of frames 3 and 7 using their respective link transformations from the base frame

$$T_{B3}\ (d_1^*, d_2^*, \theta_3^*) = T_{B0} \cdot T_{01} \cdot T_{12} \cdot T_{23} \quad (4)$$

$$T_{B7}\ (d_5^*, d_6^*, \theta_7^*) = T_{B0} \cdot T_{05} \cdot T_{56} \cdot T_{67}. \quad (5)$$

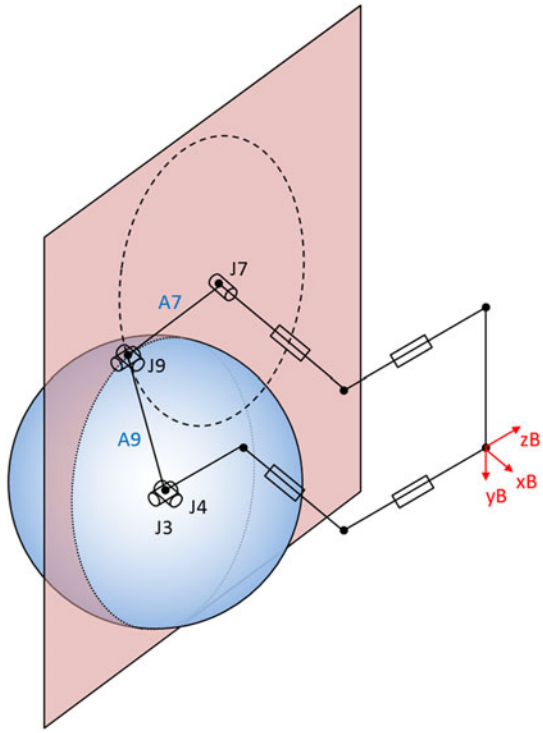

Fig. 4. Illustration of the geometric approach used to determine the manipulator's forward kinematics. The sphere represents the volume swept by the link labeled A9 centered at joints 3 and 4 (J3 and J4). The dashed circle represents the surface swept by the link labeled A7 about joint 7 (J7). The location of joint 9 (J9) is the intersection point of this sphere and circle.

Next, we find the intersection of the sphere of radius A9 centered at frame 3 and the circle of radius A7 centered at frame 7

$$(x - x_3)^2 + (y - y_3)^2 + (z - z_3)^2 = r_9^2 \quad (6)$$

$$(y - y_7)^2 + (z - z_7)^2 = r_7^2 \quad (7)$$

$$x = -d_6^* \quad (8)$$

where

$$\begin{aligned} x_3 &= -d_2^* \\ y_3 &= 0 \\ z_3 &= -d_1^* - A3 \\ r_3 &= A9 \\ y_7 &= -A5 \\ z_7 &= -d_5^* \\ r_7 &= A7 \end{aligned} \quad (9)$$

which gives

$$y_9 = y_3 + \frac{\left(R^2 - r_7^2 + P^2\right)(y_7 - y_3)}{2P^2} \pm \sqrt{R^2 - \left(\frac{R^2 - r_7^2 + P^2}{2P}\right)^2} \frac{(z_7 - z_3)}{P} \quad (10)$$

$$z_9 = z_3 + \frac{\left(R^2 - r_7^2 + P^2\right)(z_7 - z_3)}{2P^2} \mp \sqrt{R^2 - \left(\frac{R^2 - r_7^2 + P^2}{2P}\right)^2} \frac{(y_7 - y_3)}{P} \quad (11)$$

where

$$R = \sqrt{r_3^2 - \left(-d_6^* - x_3\right)^2} \quad (12)$$

$$P = \sqrt{\left(y_3 - y_7\right)^2 + \left(z_3 - z_7\right)^2} \quad (13)$$

and because of the elbow-out configuration we can always choose the smallest (most negative) y and z solutions. P is the distance between the centers of the sphere and circle. Therefore, if $P = (r_9 + r_7)$, then the robot is at a singularity point, with links A9 and A7 fully stretched out. This and $P > (r_9 + r_7)$ should never occur if the robot limits are carefully chosen.

In summary

$$(x_3, y_3, z_3) = (-d_2^*, 0, -d_1^* - A3) \quad (14)$$

$$(x_7, y_7, z_7) = (-d_6^*, -A5, -d_5^*) \quad (15)$$

$$(x_9, y_9, z_9) = (-d_6^*, (10), (11)). \quad (16)$$

And the subsequent unknown joint angles θ_3^* and θ_4^*, required to solve the forward kinematics in (1), are as follows:

$$\theta_3^* = \operatorname{asin}\left(\frac{y_9 - y_3}{\sqrt{A9^2 - \left(x_9 - x_3\right)^2}}\right) \quad (17)$$

$$\theta_4^* = \operatorname{asin}\left(\frac{x_9 - x_3}{A9}\right). \quad (18)$$

1) Robot Inverse Kinematics: The inverse kinematics can be solved in a similar geometric fashion as the forward kinematics. The solution involves working backward from the end effector and progressively locating the unknown joints variables θ_7^* and θ_9^*.

We are given the homogeneous transformation from the robot's base to the end effector

$$T_{\mathrm{Bee}} = \begin{bmatrix} R_{\mathrm{xx}} & R_{\mathrm{yx}} & R_{\mathrm{zx}} & x_{\mathrm{ee}} \\ R_{\mathrm{xy}} & R_{\mathrm{yy}} & R_{\mathrm{zy}} & y_{\mathrm{ee}} \\ R_{\mathrm{xz}} & R_{\mathrm{yz}} & R_{\mathrm{zz}} & z_{\mathrm{ee}} \\ 0 & 0 & 0 & 1 \end{bmatrix}. \quad (19)$$

The location of frame 9 can be found from the following link transformation:

$$T_{B9} = \mathrm{T}_{\mathrm{Bee}} \cdot \mathrm{T}_{4\mathrm{ee}}^{-1} \cdot \mathrm{T}_{94}^{-1} \quad (20)$$

where the transformations $\mathrm{T}_{4\mathrm{ee}}$ and T_{94} are constant, as defined in the forward kinematics (see DH parameters in Table III).

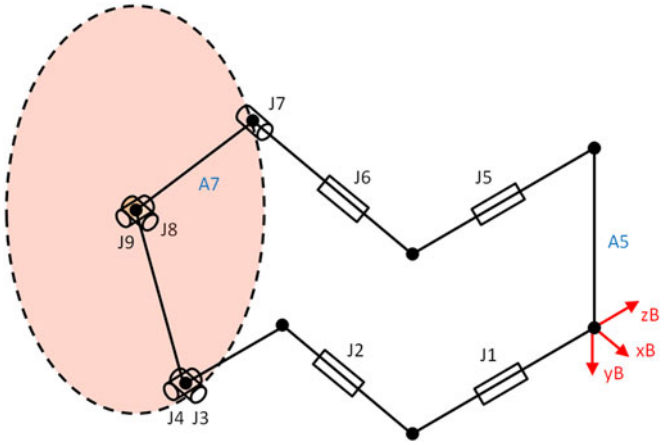

Fig. 5. Illustration of the geometric approach used to determine the manipulator's inverse kinematics. The dashed circle represents the path swept by rotating the link labeled A7 about joint 9 (J9).

As shown in Fig. 5, the location of J7 can be determined by looking at the circle described by rotating link A7 about J9. We know that the y-coordinate of frame 7 must be located at –A5, so we can solve the set of equations

$$(y - y_9)^2 + (z - z_9)^2 = A7^2 \quad (21)$$

$$y = -A5 \quad (22)$$

which gives

$$z = \sqrt{A7^2 - \left(-A5 - y_9\right)^2} + z_9. \quad (23)$$

The location of frame 7 is therefore

$$(x_7, y_7, z_7) = (x_9, -A5, (23)). \quad (24)$$

The actuated joint variables can then be easily found from the locations of the end effector and frame 7

$$d_1^* = -(z_{\mathrm{ee}} + A3) \quad (25)$$

$$d_2^* = -x_{\mathrm{ee}} \quad (26)$$

$$d_5^* = -z_7 \quad (27)$$

$$d_6^* = -x_{7.} \quad (28)$$

D. Fiducial Segmentation and Robot Registration

In order to locate the robot in the CT and MR image volumes, fiducials were incorporated into the structure of the robot, allowing fully automatic segmentation and registration. The two planar fiducials were included on the insertion module, one near the lower needle grip, and the other parallel to the first and 85 mm above it. Each fiducial was an asymmetrical and multibranched hollow shape machined into the robot's structure. For CT imaging, the shapes were left hollow, however, for MR imaging, they were filled with soft PVC material, visible in both T1 and T2-weighted sequences. PVC was used because the fiducials in this prototype were difficult to seal and water-based solutions tended to evaporate over time. As will be discussed in the Discussion

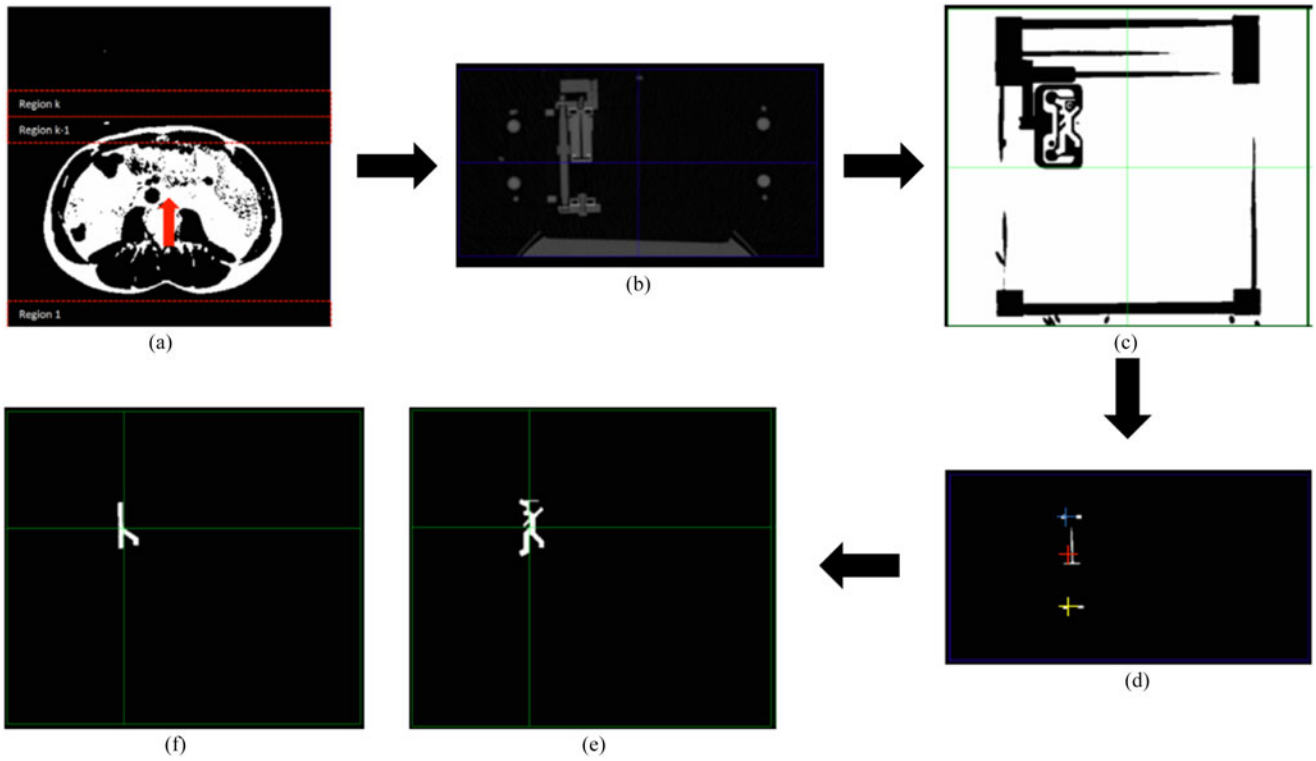

Fig. 6. Image processing steps used for automatically segmenting the fiducials from the CT images. (a) Patient anatomy is cropped by finding the top of the patient's body using a rectangular region of interest scanned from bottom to top. (b) Transverse cut of a CT image showing the cropped result. (c) Coronal cut showing the thresholded robot. (d) Volume-thresholded image showing three separate connected components with their centers marked with crosses. Coronal cut showing the resulting segmented upper (e) and lower (f) fiducials.

section, PVC was ultimately not the ideal solution, as it was affected by a chemical shift artifact in the MR images.

A segmentation routine was developed using a sequence of basic image processing techniques, allowing the fiducials to be found in standard CT and MR image volumes without the need for any user interaction. The first step is to reduce the volume size in order to speed up the subsequent steps and to allow the technique to be used on a standard laptop computer. The original 16-bit DICOM volume is therefore remapped to 8-bits and then the lower portion of the volume containing the patient anatomy is removed [see Fig. 6(b)]. To do this, a search region is swept up the central image slice from bottom to top [see Fig. 6(a)], summing the pixel intensities and giving a total intensity for each region. A sudden drop in the total intensity is used as a threshold for distinguishing the top of the patient's body.

Once the image volume has been reduced in size, it can be segmented. The cropped volume is therefore thresholded based on calibrated low and high grayscale values [see Fig. 6(c)], resulting in a black and white image containing numerous groups of pixels that could all potentially represent both the upper and lower fiducials. For CT images, the threshold range lies between 0 and 10 since the fiducial is empty. For MR images, both T1 and T2-weighted, the threshold range is from 25 to 255 since the fiducial signal is surrounded by essentially empty signals. Next, a connected components analysis is run on the thresholded image volume, grouping together all the connected white pixels. A volume thresholding is then done to exclude all the components that are either too small or too large to be either the upper or lower fiducials [see Fig. 6(d)]. The final step selecting from any remaining connected components, the two ones for which the distance between their centers of mass is 85 mm [see Figs. 6(e) and (f)]. The segmented fiducials can then be extracted into a single mesh of points and the fiducial models registered to them using the iterative closest point method.

Once the robot has been registered in the 3-D image, the radiologist can select a target and a skin insertion point. The motor positions required to align the needle with the target insertion axis need to then be determined. Fig. 7 illustrates the situation in which the needle is currently in a known position N with respect to the image frame S. Its position is defined by the transformation T^{SN} and is determined from the fiducial segmentation and registration routine described above. From the robot's forward kinematics, we also know the transformation T^{RN} from the robot's frame R to the current needle frame N. The transformation from the image frame to the robot frame is therefore:

$$T^{\mathrm{RS}} = T^{\mathrm{RN}} \cdot T^{\mathrm{SN}^{-1}}. \tag{29}$$

We can now use this transformation to determine by how much the motors must be moved to align the needle with the target axis A. The target axis is defined in image coordinates by the chosen target point inside the patient, which we will call P^S, and the unit vector $\vec{V}^S$ joining the target and skin insertion points. We can express these in robot coordinates through the

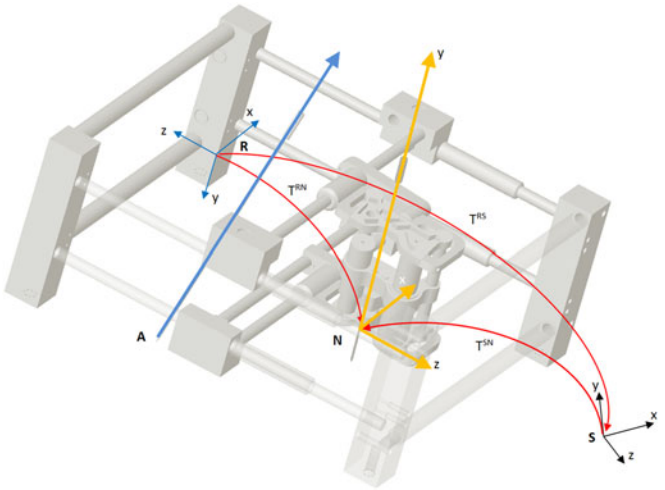

Fig. 7. Transformations between image (S), robot (R), and current needle (N) frames that are required to determine how to position the robot's motors in order to align the needle with the target insertion axis (A).

following transformations:

$$P^R = T^{\mathrm{RS}} \cdot P^S \tag{30}$$

$$\vec{V}^R = T^{\mathrm{RS}} \cdot \vec{V}^S. \tag{31}$$

We can now find the intersection between the axis A and the plane formed by the x- and z-axes of the robot frame, which is where the robot's end effector will have to be positioned. To do so, we can define the axis A by the following parametric equations:

$$x - P_x^R = t \cdot \vec{V}_x^R \tag{32}$$

$$y - P_y^R = t \cdot \vec{V}_y^R \tag{33}$$

$$z - P_z^R = t \cdot \vec{V}_z^R. \tag{34}$$

Since the xz plane of the robot is at $y = 0$, we can solve for t

$$t = -\frac{P_y^R}{\vec{V}_y^R}. \tag{35}$$

Giving us the desired robot end effector coordinates in the robot frame of reference

$$\begin{aligned} x &= P_x^R + P_y^R \frac{\vec{V}_x^R}{\vec{V}_y^R} \\ y &= 0 \\ z &= P_z^R + P_y^R \frac{\vec{V}_z^R}{\vec{V}_y^R} y = 0. \end{aligned} \tag{36}$$

We can then use the robot's inverse kinematics to determine how to move the motors.

E. User Interface and Workflow

A user interface was designed for the system in C++ and using QT, VTK, ITK, and CamiTK [13]. CamiTK is an open-source, multiplatform modular toolkit developed in our laboratory and specifically designed for computer-assisted medical intervention software prototyping. It consists of a common core onto which users can plug self-programmed extensions, allowing them to be shared by others without the need for reprogramming.

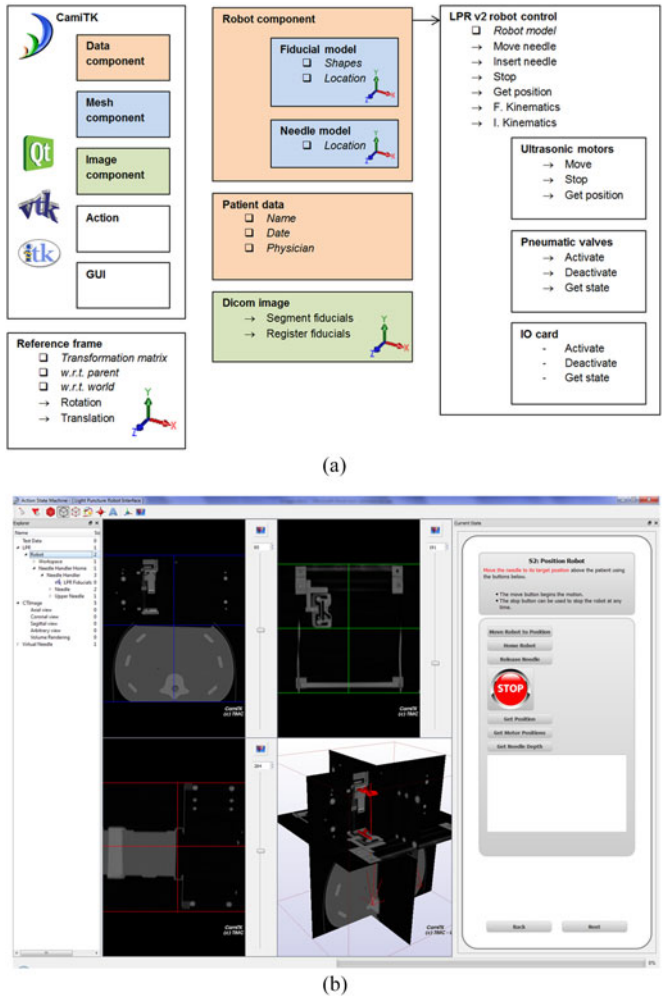

Fig. 8. (a) Block diagram showing the various elements making up the software structure of the LPR robot. (b) Screenshot of the GUI used to control the LRP system during the phantom tests, including an explorer toolbar, medical image viewer, current state description and actions, and Next and Back buttons to transition between states.

As shown in Fig. 8(a), CamiTK acts as the core of the LPR software, linking all the various elements together and allowing a number of data, mesh, and image components to be created. The Robot component is a generic component that holds the model of the fiducials and the current needle location. The Patient data component holds the information entered by the user pertaining to the current patient or test. The Dicom image component allows the images coming from the scanner to be opened and visualized. Reference frames are attached to the three visible components in order to allow them to interact together in the GUI. A library of C++ classes was also written to control this specific prototype, including a class for communicating with the robot's input/output card, a low-level motor class instantiated as five Shinsei motors within a high-level robot class for

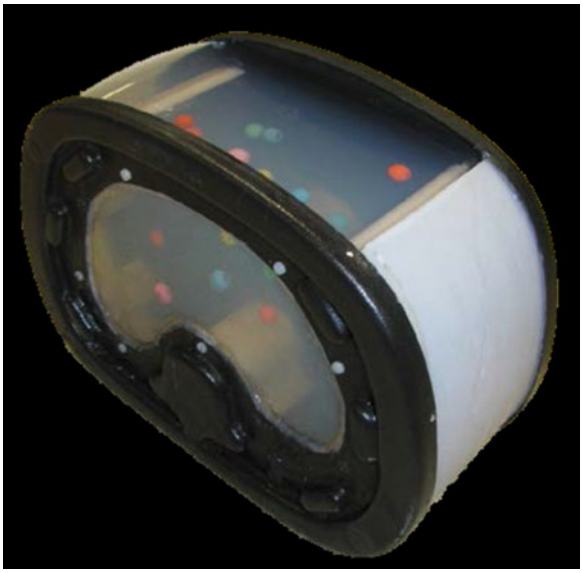

Fig. 9. Photograph of the phantom constructed for the LPR system's accuracy tests.

controlling the robot as a whole. The latter class included control commands, kinematics, and workspace definitions. This library communicates with the generic Robot component, allowing its methods to be accessed from the GUI by the user.

A GUI extension plugged into CamiTK was created that is based on the Unified Modeling Language state machine concept. It consists of a set of screens that each represents a stable state. Transitions are defined to move between states, obliging the user to follow the predefined protocol. The states and transitions were translated into an XML document, which could then be fed into the CamiTK state machine viewer. A sample screen is shown in Fig. 8(b). The segmentation and registration routine described in the previous section was programed into a CamiTK module and was applied here as a single transition.

The goal of this software structure was to keep it generic and modular in order to make it transposable to any future prototypes of the robot.

III. Methods

Phantom experiments were carried out to determine the accuracy of this new LPR prototype. They also allowed the feasibility of the robotic protocol to be verified in preparation for tests on humans. The experiments consisted of inserting a needle into a gelatin phantom with numerous targets embedded throughout. The phantom was constructed from the skeleton of an old CIRS thoracic phantom, as pictured in Fig. 9. The structure was sealed all around, leaving the top open, and a viewing window was created on one side. Seven millimeter diameter plastic beads were strung throughout the interior on nylon thread, and the phantom was then filled with alimentary gelatin and set in the fridge overnight. Gelatin was used because of the very low resistance required to puncture it with a needle, eliminating needle bending and target motion issues. Once the gelatin was set, 1-mm-diameter glass beads were distributed throughout the phantom by inserting them through a hollow needle. The large plastic beads were intended to represent more clinically feasible targets, while the small glass beads were used to provide a more challenging target. The phantom was then placed within a plastic frame upon which the robot could be solidly mounted.

The CT experiments were done using a Siemens Somatom Sensation 16 CT scanner. The characteristics of all the performed insertions are summarized in Table IV. A total of ten insertions were done, six of these using the finest slice thickness available on the imager (0.75 mm) and the rest using a coarser, more clinically viable thickness (3 mm). All insertions done with the fine images used the 1-mm-diameter glass beads as targets. The insertions done with coarse images used the more realistic-sized 7 mm plastic beads, along with one deep glass bead target for the challenge.

The MRI experiments were done using a Philips Ingenia 1.5 T wide-bore scanner, with a bore diameter of 70 cm. Only three insertions were done, one using T1-weighted images and the other two using T2-weighted images. It was not possible to obtain further results because of availability constraints on this hospital MRI machine. To improve fiducial visualization in the scanner, in addition to the MRI's main body antenna, a pair of small doughnut-shaped Philips Flex M antennas were fixed to the side of the robot. Due to the 5.3 mm image spacing of these images, only the larger plastic beads were targeted.

The procedure used for all insertions was identical and constrained to the steps defined by the GUI state machine. The robot was installed over the phantom on the scanner bed as shown in Figs. 10 and 11. A first image was taken of the entire robot and phantom. Random target and skin insertion points were chosen in this first image. The robot moved the needle automatically to the position above the insertion point. A second control image was then taken for postexperiment analysis purposes only. This second image was not used to readjust the needle position, as the goal of the study was to determine the system's accuracy based on a single image, without any user-induced corrections (i.e., the worst-case situation); it was only taken for postexperiment analysis and to adhere to the defined clinical protocol. The needle was then automatically inserted to the calculated depth and a final high-resolution image was taken. The DICOM images created by the imager during the experiments were directly passed to the robot control PC via a DICOM server. The needle used in all the experiments consisted of a 2-mm-diameter carbon fiber rod, with its end sharpened into a conical tip. This was used instead of a metallic needle in order to eliminate image artifacts that would hinder the postexperiment analysis in both modalities.

The accuracy measurements were done on the final image of each test. In the CT tests, this image had the same characteristics as images 1 to 6 in Table IV; in other words, a voxel size of 0.67 mm $\times 0.67$ mm $\times 0.6$ mm. In the MRI tests, image size and resolution were identical among all three images for each experiment, as described in Table IV; in other words, a voxel size of 0.73 mm $\times$ 0.73 mm $\times$ 5.3 mm for the T1 sequence and 0.88 mm $\times 0.88$ mm $\times 5.3$ mm for the T2 sequences. Measurements were done for all insertions on this final image by manually segmenting the needle tip and skin insertion points in the images at high zoom. These were then compared

TABLE IV
SUMMARY OF THE CT AND MRI PHANTOM TESTS DONE WITH THE LPR SYSTEM

		Image					Target		Insertion angle	
Test #	Sequence type	Resolution (pixels)	Pixel size (mm)	Slice thickness (mm)	Slice spacing (mm)	Number of slices	Type	Depth (mm)	Transverse	Sagittal
CT										
1	Fine	512×512	0.67×0.67	0.75	0.6	501	Glass	33	9.3°	0°
2	Fine	512×512	0.67×0.67	0.75	0.6	501	Glass	43	0°	0°
3	Fine	512×512	0.67×0.67	0.75	0.6	501	Glass	48	6.3°	0°
4	Fine	512×512	0.67×0.67	0.75	0.6	501	Glass	52	5.1°	−13.3°
5	Fine	512×512	0.67×0.67	0.75	0.6	501	Glass	62	-8.6°	15.1°
6	Fine	512×512	0.67×0.67	0.75	0.6	501	Glass	88	0°	0°
7	Coarse	512×512	0.67×0.67	3	2	151	Plastic	27	2.9°	−13.0°
8	Coarse	512×512	0.67×0.67	3	2	151	Plastic	51	0.7°	0°
9	Coarse	512×512	0.67×0.67	3	2	151	Plastic	73	−5.8°	0°
10	Coarse	512×512	0.67×0.67	3	2	151	Glass	92	0°	0°
MRI										
1	T1	480×480	0.73×0.73	5	5.3	35	Plastic	27	−1.5°	0°
2	T2	480×480	0.88×0.88	5	5.3	35	Plastic	48	0°	0°
3	T2	480×480	0.88×0.88	5	5.3	35	Plastic	55	0.9°	0°

The tests are organized by slice spacing and increasing insertion depth. All image volumes consisted of transverse slices. The MRI images had the following additional characteristics: T1-weighted (TR = 502 ms, TE = 10 ms, flip angle = 90°), T2-weighted (TR = 1158 ms, TE = 80 ms, flip angle = 90°). Transverse angles are in plane with the image slices and sagittal angles are in the slice-thickness direction.

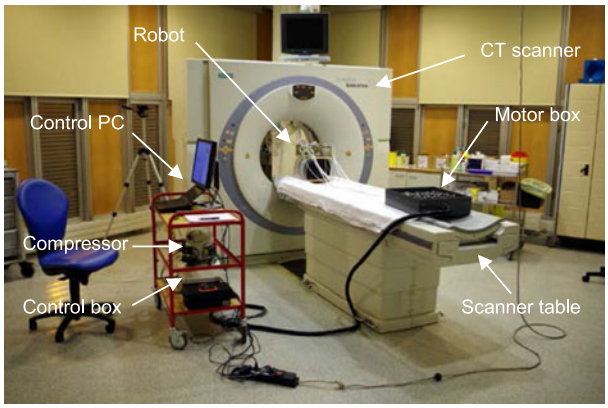

Fig. 10. Photograph of the phantom experiment setup in the CT scanner room. The robot is placed over the phantom at the head of the scanner table. The motor box is placed at the feet of the scanner table. The work area, including control PC, control box, and a compressor were placed within the imaging room in order to have a closer view of the robot motions during the experiments.

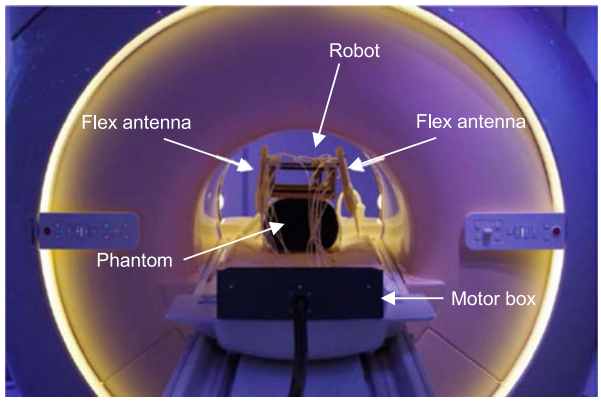

Fig. 11. Photograph of the phantom experiment setup in the MRI scanner room. Here, we see the robot and phantom within the scanner bore with the motor box in the foreground well outside the tunnel and the two Flex antennas installed on the side of the robot. The work area, including control PC, control box and compressor were all outside the imaging room.

with the planned target and insertion points projected onto this final image. This projection could be done because the final image was taken in the exact same spatial configuration as the first image, without moving the robot or phantom on the scanner bed.

A visual check of whether the needle hit the target was also done through the phantom's window to give a visual qualitative result of whether the target was hit. The distance between the needle tip and the planned target position was measured, as was the distance between the actual and planned insertion points. A point high up on the needle was also segmented, allowing the calculation of the resulting needle angles in the transverse and sagittal planes. These angles were compared to their respective planned angles.

The images acquired during the CT tests were also used to analyze the accuracy and repeatability of the fiducial segmentation and registration technique. As can be seen in Fig. 12, the measurement was done by looking at the imaging plane parallel to each fiducial and comparing the actual visible needle position to the registered needle position. Segmentation of the needle in the image was done manually. A total of 16 CT images with a slice spacing of 0.6 mm, and eight images with a slice spacing of 2.0 mm were used. This registration error could not be measured in the MRI images because the needle was not visible in air.

IV. RESULTS

The results of the CT and MRI experiments are shown in Tables V and VI, respectively. Of the seven 1-mm-diameter glass beads targeted under CT guidance, three were actually hit by the needle. All 7-mm-diameter plastic beads were hit in both modalities.

TABLE V
RESULTS OF THE CT PHANTOM TESTS

		Target			Target error (mm)				Angle error	
Test #	Image type	Type	Depth (mm)	Hit?	x	y	z	E	Transverse	Sagittal
CT										
1	Fine	Glass	33	No	3.3	3.3	−0.6	4.7	1.5°	−0.2°
2	Fine	Glass	43	Yes	1.3	1.3	1.2	2.2	0.8°	0.4°
3	Fine	Glass	48	No	2.0	3.3	0.0	3.9	0.8°	−0.2°
4	Fine	Glass	52	No	0.0	2.0	−3.0	3.6	2.0°	−0.2°
5	Fine	Glass	62	Yes	1.3	3.3	0.0	3.6	0.4°	0.2°
6	Fine	Glass	88	No	3.3	6.0	0.6	6.9	1.5°	0.2°
7	Coarse	Plastic	27	Yes	1.3	1.3	−3.0	3.5	0.6°	−0.8°
8	Coarse	Plastic	51	Yes	−0.7	0.0	−0.2	0.7	0.1°	−0.6°
9	Coarse	Plastic	73	Yes	−1.3	-0.7	0.6	1.6	−0.2°	−0.4°
10	Coarse	Glass	92	Yes	0.7	-0.7	2.4	2.6	0.6°	0.2°
Total Mean					**1.1 ± 1.5**	**1.9 ± 2.1**	**-0.2 ± 1.7**	**3.3 ± 1.7**	**0.8 ± 0.7°**	**–0.1 ± 0.4°**

Target error is the distance measured between the segmented needle tip and the planned target position. Angle error is the angular distance between the segmented needle axis and the planned needle direction. The *x*- and *y*-axes are the horizontal and vertical directions in the transverse imaging plane and the *z*-axis is in the slice-width (tunnel) direction. E stands for the Euclidean distance. In the Image type column, Fine refers to the images with 0.6 mm slice spacing while Coarse refers to the images with 2 mm slice spacing. Means and standard deviations are shown in bold font.

TABLE VI
RESULTS OF THE MRI PHANTOM TESTS

		Target			Target error (mm)				Angle error	
Test #	Image type	Type	Depth (mm)	Hit?	x	y	z	E	Transverse	Sagittal
MRI										
1	T1	Plastic	27	Yes	−0.7	−1.5	0.0	3.1	−1.5°	0.0°
2	T2	Plastic	48	Yes	−1.8	−0.9	0.0	2.0	−1.6°	0.0°
3	T2	Plastic	55	Yes	0.4	0.0	0.0	0.4	−0.5°	0.0°
Mean					**–0.7 ± 1.1**	**–0.8 ± 0.7**	**0.0 ± 0.0**	**1.3 ± 0.8**	**–1.2 ± 0.6°**	**0.0 ± 0.0°**

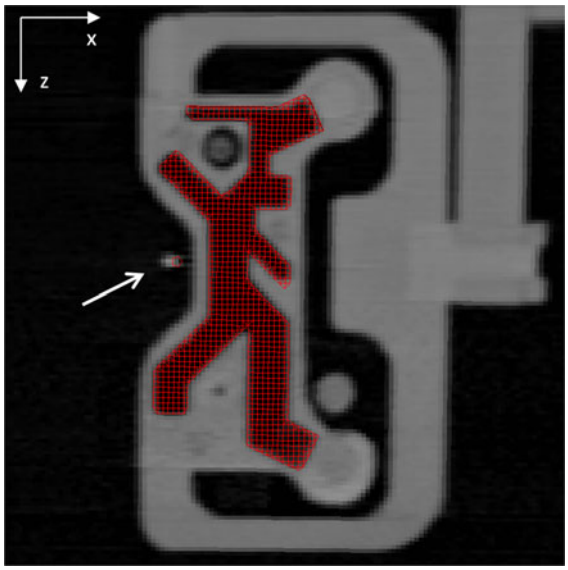

Fig. 12. Location of the needle (marked by arrow) with respect to the upper fiducial in a CT image. The registered fiducial model is overlaid in red with the registered needle location shown as a faint circle beside the white spot of the actual needle in the image. Note the misalignment in the *x*-direction of the visible white needle compared to the registered red needle, as explained in the text.

In the CT experiments, insertion depths ranged from 30 to 90 mm. The overall mean error between the final needle tip location and the planned target position was 3.3 mm $\pm$ 1.7 mm. The overall mean error at the "skin" insertion point was 1.7 mm $\pm$ 0.9 mm. The overall transverse and sagittal angular errors were $0.8 \pm 0.7^\circ$ and $-0.1 \pm 0.4^\circ$, respectively. The total mean error in the *y* (depth) direction was the greatest, the error in the *x* (transverse, horizontal) direction was also >1 mm, while the error in the *z*-direction was fairly low. Naturally, since the errors in the *x*-direction were larger than in the *z*-direction, the transverse angle error (about the *z*-axis) was greater than the sagittal (about the *x*-axis) error. Looking at the first six insertions that used finely-spaced images, errors tend to increase with depth, except for the first insertion, which was the farthest away from the robot's home position.

In the MRI experiments, the overall mean target error in the transverse plane was 1.3 mm $\pm$ 0.8 mm, while the transverse angular error was $-1.2 \pm 0.6^\circ$. Note that the zero error in the *z*-(slice-depth) direction, as seen at the bottom of Table VI, is not representative due to the very large slice spacing of the images (over twice the size of the needle's diameter). This made any needle tip errors in the *z*-direction impossible to distinguish. The Euclidean error of the MRI results should not therefore be compared to the CT results. To measure the *z*-error, we could have either scanned the phantom after each needle insertion

TABLE VII
MEAN ERROR BETWEEN THE REGISTERED NEEDLE LOCATION AND THE NEEDLE SEGMENTED IN THE CT IMAGES

Image resolution (mm)	Fiducial	Registration error (mm) x	y	z	E
$0.67 \times 0.67 \times 0.6$	Upper	1.26 ± 0.29	-0.14 ± 0.34	-0.31 ± 0.37	1.39 ± 0.33
	Lower	1.39 ± 0.19	-0.10 ± 0.18	-0.18 ± 0.23	1.43 ± 0.21
$0.67 \times 0.67 \times 2.0$	Upper	1.27 ± 0.35	-0.06 ± 0.25	-1.06 ± 0.85	1.86 ± 0.30
	Lower	1.40 ± 0.17	0.03 ± 0.12	-0.66 ± 1.07	1.84 ± 0.22

with a CT scanner with fine slice thickness or we could have done a high-resolution control MRI image after each insertion. Unfortunately, we did not have sufficient time available on these clinical machines to allow us to acquire these images.

Timewise, the procedure between the acquisition of the first image and the acquisition of the final image was typically about 20 min for the CT experiments and on the order of 30 to 45 min for the MRI experiments. The time for just the automatic fiducial segmentation and registration procedure was on the order of 40 s for the biggest size CT images, and dropping to 3 s for the smallest size MRI images. These times were measured on the robot control laptop, which consisted of a 2.80 GHz Intel Core i7 processor, 8 Gb of RAM and a 64-bit Windows 7 Professional operating system.

The fiducial segmentation and registration accuracy measurements gave the results shown in Table VII. The main registration error was in the *x*-direction (see Fig. 12 for direction). This was an error found only after the phantom experiments and consisted of an inaccuracy in the model's distance between the needle axis and the fiducial (constructed from the original CAD model of the robot). The mean registration error over all the CT images, including the large systematic error in the *x*-direction, was 1.54 mm ± 0.33 mm.

V. DISCUSSION

The phantom experiments showed that the LPR system is feasible as a potentially fast and reliable way of inserting needles to varying depths in a patient, along any inclination both in and out of the imaging plane and using the same procedure in both CT and MRI modalities.

The desired accuracy of the LPR system depends on the minimal size of lesion that the system is likely to be used on. Lesion size is not the only criterion used to determine whether a lesion requires IR-based diagnosis or treatment. Other criteria, such as lesion location, dispersion, density, appearance, growth rate, patient symptoms, and patient history, are important in the clinician's decision. It is difficult, therefore, to pinpoint an exact minimum lesion size that the system would be expected to deal with, in particular because of the large array of IR procedures accessible to the system. Since the needle trajectory often passes near neighboring vital tissues, the needle's orientation accuracy is also important. According to our partner radiologists, the minimum size of lesion likely to be targeted using CT or MRI is 10 mm in diameter, although this depends highly on the organ and clinical problem. Smaller lesions can be difficult to locate in the images and are generally not considered clinically serious enough to warrant invasive diagnosis or treatment. We, therefore, chose a desired accuracy of less than 5 mm, which would allow lesions with at least a 10 mm diameter to be successfully targeted. The phantom experiments showed that both the target and "skin" insertion point accuracies lay within this 5 mm objective for varying image resolutions, needle depths, inclinations and for both CT and MRI guidance.

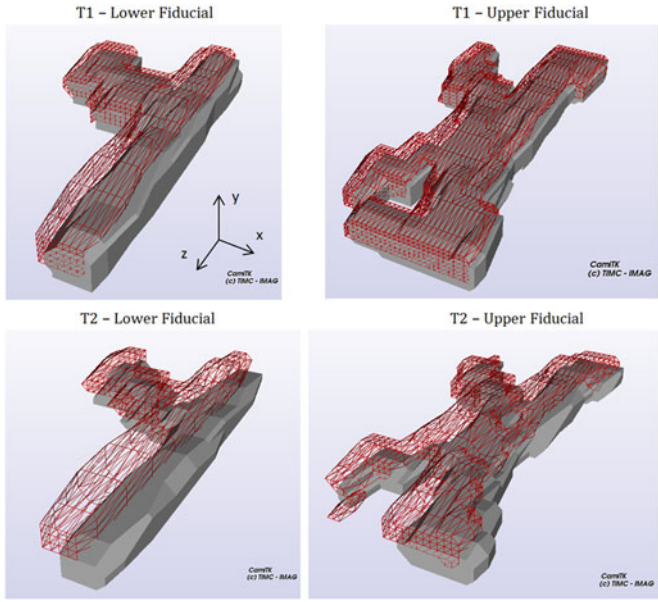

Fig. 13. Segmented fiducials from images with swapped frequency and phase encoding directions overlaid one (red mesh) on top of the other (gray mesh) to show the chemical shift between them. A shift in the *x*- and the *y*-directions is present, depending on the frequency encoding direction of each image.

Although the 5 mm objective was achieved, a number of sources of error were discovered during postanalysis that could improve the system's overall error. The systematic geometrical error in the x-direction, described at the end of the Results section could be easily rectified, improving the system's final accuracy. In addition, for the MRI tests, another important error was discovered after completion of the experiments because the PVC, oil-based fiducials were subject to a chemical shift artifact. Chemical shift artifacts result from a slight difference in a material or tissue's resonant frequency, causing a miscalculation of its position in the frequency-encoding direction. Indeed, an article was published on the subject in 1997 by Condon and Hadley, specifically for soft PVC materials, showing a shift of 2.4 mm [14]. We did our own tests to determine the shift of our fiducials by taking two identical images with their frequency and phase encoding directions switched. We did this for both the T1 and T2 images done in our experiments. Fig. 13 shows the resulting segmented fiducials overlaid one on top of the other. The shift of the fiducials' centers of mass in the x(frequency encoding)-direction are shown in Table VIII and are on the order of 1.5 mm in T1 images and 2 mm in T2 images in the

TABLE VIII
CHEMICAL SHIFT IN THE *x*-DIRECTION OF THE UPPER AND LOWER FIDUCIALS

Image type	Fiducial	Shift (mm)
T1	Upper	−1.51
	Lower	−1.24
T2	Upper	−1.94
	Lower	−2.28

The shift was determined by measuring the difference between the centers of mass of the segmented overlapping fiducials.

negative x-direction. This can explain the negative *x*-errors in the MRI targeting results in Table VIII.

Experimental errors extrinsic to the actual system's accuracy also need to be considered when looking at the results. These were primarily limited to the segmentation of the needle tip in the final image. This segmentation was done manually and was therefore prone to human error. It was dependent 1) on the image resolution and 2) on the judgment made in choosing the actual pixel that represented the needle tip. The image resolution could have caused an error of up to 1 voxel. The maximum distance between two voxel centers in the fine CT images used to segment the needle tips was 1.1 mm. In the MRI images, as mentioned earlier, only the errors in the transverse slices are representative. The image resolution error in the transverse direction for the T1 and T2 images is 1.0 and 1.2 mm, respectively. The judgment error in choosing the actual needle tip was based on determining where along the length of the needle the tip actually lay. The choice of needle tip typically spanned between at least 2 voxels. An estimate of the judgment error would therefore be the distance between two voxels, i.e., the same as the image resolution error. The total estimated RMS error in the segmentation of the needle tip in the CT images is therefore 1.6 mm, while the error in the transverse plane of the T1 and T2 images is 1.5 and 1.8 mm, respectively. These experimental errors therefore play a large role in the overall 3.3 and 1.3 mm accuracies measured during the CT and MRI experiments, respectively.

With regards to the clinical pertinence of these experiments, it is important to note that needle-tissue interaction effects were not considered because the experimental protocol was based on the same assumptions as those used by radiologists in the standard manual technique; that is, that the needle enters the tissue without bending and without deforming the tissue. Corrections for these interaction errors are done in an adaptive manner after insertion, rather than predictively before insertion.

In addition, all the insertions were based on one single initial image. No control corrections were done on subsequent images to ensure that the needle was properly aligned with the desired trajectory, which is not clinically reasonable. In reality, the second image would be used to control the current needle position with respect to the initial planned trajectory, and the position would be corrected if deemed necessary by the radiologist. This would have improved the system's accuracy, depending on how many corrections were made. Indeed, this is the strength of the robot, because although it can do automatic motions, in the end, the desired accuracy is chosen by the radiologist based on what he or she sees and evaluates in the image. For these experiments, however, we wished to determine the robot's accuracy alone, without any user input that would improve its chances of doing better.

An important limitation to this study was the small number of MRI insertions done. The CT and MRI tests were both done in clinically active imaging machines, in between patients, and MRI-time in particular was very limited. The goal of the MRI tests reported here were to evaluate the preliminary feasibility of using the robot and the clinical protocol in the MRI. Based on these results, we were subsequently able to put in place an official ethics-approved study in the MRI on human subjects with dedicated MRI-time. The results will be described in a subsequent publication.

Some improvements could be made to this prototype to further improve its accuracy and reliability. First and foremost, the manufacturing tolerances in the joints of this particular prototype could be significantly improved, reducing play and making joint calibration and repeatability much more accurate. In a clinical setting, insertion forces would be greater than in the gelatin experiments described, so joint rigidity would be an important aspect to improve upon.

In addition, the use of Bowden cables to actuate the robot means that inaccuracies due to cable stretch must be reduced. These inaccuracies occur because as the motors start to pull on the cables, there is a latency and inaccuracy in the subsequent robot joint motion at the other end of the cables. This is caused by the stretch of the cables and housing as they overcome the static friction in the system. In the current prototype, the hysteresis caused by cable stretch was mitigated by adding or subtracting an offset distance to the motor position commands whenever a change in direction occurred for each motor. This offset distance was calibrated for each motor prior to each experiment by applying motions to the motors and measuring the resulting difference at each prismatic joint with a caliper. Tests were done to determine the accuracy and repeatability of the calibrated offsets by moving each joint to a same position a number of times and taking manual caliper measurements. The results for the four position motors were <0.5 mm. The fifth motor, used to adjust the insertion depth, was verified by inserting a needle to a depth of 80 mm at a stroke depth of 20 mm and the resulting tip depth was measured. The accuracy and repeatability over 20 insertions was also <0.5 mm. Extrapolating these joint errors down to a needle depth of 90 mm (maximum depth attained during the phantom tests) would result in a needle-tip accuracy in air of 2 mm. This accuracy could be improved by incorporating an automated calibration routine that would allow to map the offset amount throughout the robot's workspace. Automation could be done using a position tracker such as an NDI Polaris optical tracker.

VI. CONCLUSION

In this paper, we describe a CT- and MRI-compatible IR robot whose novelty lies in a number of aspects. First, its multimodality greatly opens up its expected clinical benefit,

providing radiologists with a versatile tool that can be used to take advantage of both CT and MRI imaging particularities. Its fixation on the patient's body allows it to move with the patient, improving safety and comfort. The use of offset motors allows the robot structure to be lighter and less prone to image artifacts. Its accuracy and fully automatic registration routine could allow the robot to be used in more complex situations, in which out-of-plane needle inclinations and close insertion tolerances are required. It would also potentially reduce the number of images required to reach the target, reducing the number of breath-holds required by the patient, decreasing the radiation exposure in CT interventions, eliminating the need for the radiologist to come and go between the patient and the control room, and shortening the overall procedure time. Finally, with regards to MRI, it could open up the possibility of doing interventions that currently are not technically feasible given the magnetic and space constraints of standard MRI machines.

REFERENCES

[1] A. Krieger, G. Metzger, G. Fichtinger, E. Atalar, and L. L. Whitcomb, "A hybrid method for 6-DOF tracking of MRI-compatible robotic interventional devices," in *Proc. IEEE Int. Conf. Robot. Autom.*, Orlando, FL, USA, 2006, pp. 3844–3849.

[2] A. Melzer *et al.*, "INNOMOTION for percutaneous image-guided interventions: principles and evaluation of this MR- and CT-compatible robotic system," *IEEE Eng. Med. Biol. Mag.*, vol. 27, no. 3, pp. 66–73, May/Jun. 2008.

[3] E. G. Christoforou, I. Seimenis, E. Andreou, E. Eracleous, and N. V. Tsekos, "A novel, general-purpose, MR-compatible, manually actuated robotic manipulation system for minimally invasive interventions under direct MRI guidance," *Int. J. Med. Robot. Comput. Assist. Surg.*, vol. 10, no. 1, pp. 22–34, Apr. 2013.

[4] D. J. van Gerwen, J. Dankelman, and J. J. van den Dobbelsteen, "Needle–tissue interaction forces - A survey of experimental data," *Med. Eng. Phys.*, vol. 34, no. 6, pp. 665–680, Jul. 2012.

[5] C. J. Walsh, N. C. Hanumara, A. H. Slocum, J. A. Shepard, and R. Gupta, "A patient-mounted, telerobotic tool for CT-guided percutaneous interventions," *J. Med. Devices*, vol. 2, Mar. 2008, Art. no. 011007.

[6] G. Kronreif, M. Fürst, W. Ptacek, M. Kornfeld, and J. Kettenbach, "Robotic system for image guided therapie—B-RobII," presented at the Int. Workshop Robotics Alpe-Adira-Danube Region, Balaton, Hungary, 2006.

[7] I. Bricault *et al.*, "A light puncture robot for CT and MRI interventions: Designing a new robotic architecture to perform abdominal and thoracic punctures," *IEEE Eng. Med. Biol. Mag.*, vol. 27, no. 3, pp. 42–50, May/Jun. 2008.

[8] E. Taillant, J. C. Avila-Vilchis, C. Allegrini, I. Bricault, and P. Cinquin, "CT and MR compatible Light Puncture Robot : architectural design and first experiments," in *Proc. 7th Int. Conf. Med. Image Comput. Comput.-Assisted Intervention*, Saint-Malo, France, 2004, pp. 145–152.

[9] N. Zemiti, I. Bricault, C. Fouard, B. Sanchez, and P. Cinquin, "LPR: A CT and MR-compatible puncture robot to enhance accuracy and safety of image-guided interventions," *IEEE/ASME Trans. Mechatronics*, vol. 13, no. 3, pp. 306–315, Jun. 2008.

[10] N. Hungr, C. Fouard, A. Robert, I. Bricault, and P. Cinquin, "Interventional radiology robot for CT and MRI guided percutaneous interventions," in *Proc. Int. Conf. Med. Image Comput. Comput.-Assisted Intervention*, Toronto, ON, Canada, 2011, pp. 137–144.

[11] N. Hungr, "Design and evaluation of robotic systems for medical image guided percutaneous needle interventions," M.S. thesis, TIMC-IMAG Lab., Université de Grenoble, Grenoble, France, 2014.

[12] J. J. Craig, *Introduction to Robotics Mechanics and Control*, 3rd ed. Upper Saddle River, NJ, USA: Pearson Education, Inc., 2005.

[13] E. Promayon *et al.*, "Using CamiTK for rapid prototyping of interactive computer assisted medical Intervention applications," in *Proc. IEEE Conf. Eng. Med. Biol. Soc.*, Osaka, Japan, 2013, pp. 4933–4936.

[14] B. R. Condon and D. M. Hadley, "Solid localization marker for MR imaging," *Radiology*, vol. 204, no. 2, pp. 577–580, Aug. 1997.

[15] J. Kettenbach *et al.*, "Robot-assisted biopsy using ultrasound guidance: Initial results from in vitro tests," *Eur. Radiol.*, vol. 15, no. 4, pp. 765–771, Apr. 2005.

[16] G. Fichtinger *et al.*, "Robotic assistance for ultrasound guided prostate brachytherapy," in *Proc. Int. Conf. Med. Image Comput. Comput.-Assisted Intervention*, Nice, France, 2007, pp. 119–127.

[17] G. Fichtinger *et al.*, "Robotic assistance for ultrasound-guided prostate brachytherapy," *Med. Image Anal.*, vol. 12, no. 5, pp. 535–545, Oct. 2008.

[18] D. Y. Song *et al.*, "Robotic needle guide for prostate brachytherapy: Clinical testing of feasibility and performance," *Brachytherapy*, vol. 10, no. 1, pp. 57–63, Jan./Feb. 2011.

[19] B. Schulz *et al.*, "Accuracy and speed of robotic assisted needle interventions using a modern cone beam computed tomography intervention suite: a phantom study," *Eur. Radiol.*, vol. 23, no. 1, pp. 198–204, Jan. 2013.

[20] D. Stoianovici *et al.*, "An efficient needle injection technique and radiological guidance method for percutaneous procedures," in *Proc. 1st Joint Conf. Comput. Vis., Virtual Reality Robot. Med. Med. Robot. Comput.-Assisted Surgery*, Grenoble, France, 1997, pp. 295–298.

[21] D. Stoianovici, L. L. Whitcomb, J. H. Anderson, R. H. Taylor, and L. R. Kavoussi, "A modular surgical robotic system for image guided percutaneous procedures," in *Proc. 1st Int. Conf. Med. Image Comput. Comput.-Assisted Intervention*, Cambridge, MA, USA, 1998, pp. 404–410.

[22] A. Patriciu *et al.*, "Motion-based robotic instrument targeting under C-Arm fluoroscopy," in *Proc. 1st Int. Conf. Med. Image Comput. Comput.-Assisted Intervention*, Pittsburgh, PA, USA, 2000, pp. 988–988.

[23] K. Masamune *et al.*, "System for robotically assisted percutaneous procedures with computed tomography guidance," *Comput. Aided Surg.*, vol. 6, no. 6, pp. 370–383, 2001.

[24] G. Fichtinger *et al.*, "System for robotically assisted prostate biopsy and therapy with intraoperative CT guidance," *Acad. Radiol.*, vol. 9, no. 1, pp. 60–74, Jan. 2002.

[25] D. Stoianovici *et al.*, "AcuBot: A robot for radiological interventions," *IEEE Trans. Robot. Autom.*, vol. 19, no. 5, pp. 927–930, Oct. 2003.

[26] K. Cleary *et al.*, "Precision placement of instruments for minimally invasive procedures using a "Needle Driver" robot," *Int. J. Med. Robot. Comput. Assist. Surg.*, vol. 1, no. 2, pp. 40–47, Jan. 2005.

[27] S. Shah *et al.*, "Robotically assisted needle driver: evaluation of safety release, force profiles, and needle spin in a swine abdominal model," *Int. J. Comput. Assist. Radiol. Surg.*, vol. 3, nos. 1/2, pp. 173–179, Jun. 2008.

[28] R. Pollock *et al.*, "Prospects in percutaneous ablative targeting: Comparison of a computer-assisted navigation system and the acubot robotic system," *J. Endourol.*, vol. 24, no. 8, pp. 1269–1272, Aug. 2010.

[29] M. H. Loser and N. Navab, "A new robotic system for visually controlled percutaneous interventions under CT fluoroscopy," in *Proc. 3rd Int. Conf. Med. Image Comput. Comput.-Assisted Intervention*, Pittsburgh, PA, USA, 2000, pp. 887–896.

[30] E. Hempel *et al.*, "An MRI-compatible surgical robot for precise radiological Interventions," *Comput. Aided Surg.*, vol. 8, no. 4, pp. 180–191, 2003.

[31] S. Zangos *et al.*, "MR-compatible assistance system for punction in a high-field system: Device and feasibility of transgluteal biopsies of the prostate gland," *Eur. Radiol.*, vol. 17, no. 4, pp. 1118–1124, Apr. 2007.

[32] S. Zangos *et al.*, "MR-compatible assistance system for biopsy in a high-field-strength system: initial results in patients with suspicious prostate lesions," *Radiology*, vol. 259, no. 3, pp. 903–910, Jun. 2011.

[33] B. Schell *et al.*, "Robot-assisted biopsies in a high-field MRI system—First clinical results," *Fortschr Röntgenstr*, vol. 184, no. 1, pp. 42–47, Jan. 2012.

[34] N. V. Tsekos, A. Özcan, and E. Christoforou, "A prototype manipulator for magnetic resonance-guided interventions inside standard cylindrical magnetic resonance imaging scanners," *J. Biomech. Eng.*, vol. 127, no. 6, pp. 972–980, Nov. 2005.

[35] E. Christoforou and N. V. Tsekos, "Robotic manipulators with remotely-actuated joints: Implementation using drive-shafts and u-joints," in *Proc. IEEE Int. Conf. Robot. Autom.*, Orlando, FL, USA, 2006, pp. 2866–2871.

[36] E. Christoforou, E. Akbudak, A. Ozcan, M. Karanikolas, and N. V. Tsekos, "Performance of interventions with manipulator-driven real-time MR guidance: Implementation and initial in vitro tests," *Magn. Reson. Imaging*, vol. 25, no. 1, pp. 69–77, Jan. 2007.

[37] N. V. Tsekos, E. Christoforou, and A. Özcan, "A general-purpose MR-compatible robotic system: Implementation and image guidance for performing minimally invasive interventions," *IEEE Eng. Med. Biol. Mag.*, vol. 27, no. 3, pp. 51–58, May/Jun. 2008.

[38] G. Cole, J. Pilitsis, and G. S. Fischer, "Design of a robotic system for MRI-guided deep brain stimulation electrode placement," in *Proc. IEEE Int. Conf. Robot. Autom.*, Kobe, Japan, 2009, pp. 4455–4456.
[39] Y. Wang, G. A. Cole, H. Su, J. G. Pilitsis, and G. S. Fischer, "MRI compatibility evaluation of a piezoelectric actuator system for a neural interventional robot," in *Proc. 31st Annu. Int. Conf. IEEE Eng. Med. Biol. Soc.*, Minneapolis, MN, USA, 2009, pp. 6072–6075.
[40] G. Cole, K. Harrington, H. Su, A. Camilo, J. Pilitsis, and G. S. Fischer, "Closed-loop actuated surgical system utilizing real-time in-situ MRI guidance," in *Proc. 12th Int. Symp. Exp. Robot.*, New Delhi and Agra, India, 2010, pp. 785–798.
[41] B. Maurin, "Conception et réalisation d'un robot d'iinsertion d'aiguille pour les procédures percutanées sous imageur scanner," Ph.D. dissertation, Inst. dept., Louis Pasteur Univ., Strasbourg, France, 2005.
[42] B. Maurin, B. Bayle, O. Piccin, J. Gangloff, M. de Mathelin, and P. Zanne, "A robotized positioning platform guided by computed tomography: Practical issues and evaluation," in *Proc. IEEE Int. Conf. Robot. Autom.*, Orlando, FL, USA, 2006, pp. 251–256.
[43] B. Maurin *et al.*, "A patient-mounted robotic platform for CT-scan guided procedures," *IEEE Trans. Biomed. Eng.*, vol. 55, no. 10, pp. 2417–2425, Oct. 2008.
[44] O. Piccin, L. Barbé, B. Bayle, and M. de Mathelin, "A force feedback teleoperated needle insertion device for percutaneous procedures," *Int. J. Robot. Res.*, vol. 28, no. 9, pp. 1154–1168, Sep. 2009.
[45] B. Maurin *et al.*, "CTBot: A stereotactic-guided robotic assistant for percutaneous procedures of the abdomen," in *Proc. SPIE*, vol. 5744, 2005, pp. 241–251.
[46] A. Seitel *et al.*, "Development and evaluation of a new image-based user interface for robot-assisted needle placements with the Robopsy system," in *Proc. SPIE*, vol. 7261, 2009, pp. 72610X-1–72610X-9.
[47] F. Wu *et al.*, "Compact, patient-mounted MRI-guided robot for accurate positioning of multiple cryoablation probes," in *Proc. 5th Nat. Image Guided Therapy Workshop*, Boston, MA, USA, 2012.

Nikolai Hungr received the graduate and the M.A.Sc. degrees in mechanical engineering from the University of British Columbia, Vancouver, BC, Canada, in 2003 and 2008, respectively. He received the Ph.D. degree from the Techniques de l'Ingénierie Médicale and de la Complexité - Informatique, Mathématiques and Applications de Grenoble Laboratory, Grenoble, France, in 2014.

During the master's program, he developed new haptic techniques for bone milling in orthopedic surgery. After his master's, he was a Research Engineer with the Techniques de l'Ingénierie Médicale and de la Complexité - Informatique, Mathématiques and Applications de Grenoble (TIMC-IMAG) Laboratory until 2010, where he was involved in a number of needle insertion robotics projects in the fields of urology and interventional radiology. He is currently a Postdoctoral Fellow at the TIMC-IMAG Laboratory, working on the clinical validation of the two robotic systems that he developed during his doctoral research.

Mr. Hungr has received a number of awards during his studies, including the Natural Sciences and Engineering Research Council of Canada Post Graduate Scholarship.

Ivan Bricault received the graduate degree in sciences and engineering from Ecole Polytechnique, Paris, France. He received the Ph.D. degree in applied mathematics and the Medical Doctor degree in 2002, with a specialization in Radiology and Medical Imaging from Grenoble University, Grenoble, France, in 1998 and 2002, respectively.

He is currently a Radiologist at Grenoble University Hospital, France and also a Professor at Grenoble Medical School. He works with the "Computer-Assisted Medical Interventions" research team in Techniques de l'Ingnierie Médicale Laboratory.

Philippe Cinquin received the Ph.D. degree in applied mathematics from the Saint-Etienne and Lyon 1 Universities, Lyon, France, in 1981.

In 1984, he launched a research team on Computer-Assisted Medical Interventions, which led to an innovative approach in surgical practice, due to the introduction of information technology in the operating room, and to four industrial startups. He is a Medical Doctor. He is currently a Professor of medical informatics in Grenoble, France, and the Director of the Techniques de l'Ingénierie Médicale et de la Complexité - Informatique, Mathématiques et Applications de Grenoble (TIMC-IMAG) Laboratory, a Research Unit of the Centre national de la recherche scientifique (CNRS) and the Université Joseph Fourier, and the Head of the Center for Technological Innovation at Grenoble's University Hospital.

Dr. Cinquin received the 1999 Maurice E. Muller Award for excellence in computer-assisted orthopaedic surgery, the CNRS Silver Medal in 2003, and the CNRS Medal of Innovation in 2013.

Céline Fouard received the M.S. degree in computer science and image analysis from the University of Bordeaux, Bordeaux, France, in 2001, and the Ph.D. degree in computer science and medical image analysis from the University of Nice Sophia Antipolis, Nice, France, in 2005.

During 2005 to 2006, she worked on image analysis at the Center for Image Analysis, Uppsala University, Uppsala, Sweden, in the field of discrete geometry. She is currently an Assistant Professor at the Techniques de l'Ingénierie Médicale et de la Complexité - Informatique, Mathématiques et Applications de Grenoble (TIMC-IMAG) Laboratory, University of Grenoble, Grenoble, France, where she is involved in teaching computer science and working on computer-assisted medical interventions.